The effect of shear thinning and walls on the sedimentation of a sphere in an elastic fluid under orthogonal shear

S. Padhy [a,*], M. Rodriguez [c], E.S.G. Shaqfeh [a,b], G. Iaccarino [a], J.F. Morris [d], N. Tonmukayakul [e]

[a] Department of Mechanical Engineering, Stanford University, Stanford, CA 94305, USA
[b] Department of Chemical Engineering, Stanford University, Stanford, CA 94305, USA
[c] Department of Mechanical Engineering, University of Michigan, Ann Arbor, MI 48105, USA
[d] Levich Institute and Department of Chemical Engineering, The City College of New York, New York, NY, USA
[e] Halliburton, Duncan, OK 73536, USA

ABSTRACT

We investigate the sedimentation of a sphere in a viscoelastic fluid with a cross-shear flow by numerical simulation. The non-Newtonian properties of the suspending fluid determine the settling rate of the sphere. Experiments [Tonmukayakul et al., US Patent Number US8,024,962(B2) (2010); van den Brule and Gheissary, J. Non-Newton. Fluid Mech. 49 (1993) 123–132] have shown the settling rate increases with increase in cross-shear Weissenberg number, Wi, in elastic guar gum solutions and decreases in Boger fluids. In the present work, simulations of a sheared viscoelastic flow past a sphere are used to study the effect of the shear-thinning and elasticity of the carrying fluid on the sphere's settling rate. The elastic guar gum solutions are modeled using the Giesekus constitutive model. The parameters are obtained by fitting the rheological data. The drag on the sphere decreases, i.e. the settling rate increases, with an increase in the shear Weissenberg number that is in qualitative agreement with the experiments. The decrease in the drag is primarily due to the decrease in the polymer drag component because of shear-thinning. This is in contrast with the increase in the drag in Boger fluids due to the increase in viscous drag. The effect of different polymer characteristics such as shear thinning and elasticity on the flow field is presented. There is an optimum value for the amount of polymers in the solution for the increase in the viscous drag to overcome the decrease in the polymer drag leading to a net increase in the drag on the sphere. The effect of walls on the drag coefficients in Boger fluids is also investigated. It is demonstrated that the effect of the increase in the drag coefficients with Wi is accentuated as the interaction with the wall grows stronger. The wall interactions lead to an increase in viscous shear stresses downstream of the sphere, which causes the increase in the drag.

© 2013 Elsevier B.V. All rights reserved.

1. Introduction

The understanding of suspensions of particles in viscoelastic fluids is essential for many engineering applications [1]. One of the applications of interest is in the hydraulic fracturing used during drilling of oil and gas wells [2]. Suspensions of solids in polymeric solutions are pumped during the drilling process to prop open the fracture for enhanced oil recovery. These solids, known as 'proppant', play an essential role in the hydraulic fracturing process. The solids are usually dense mineral particles like sand or sintered bauxite. Sedimentation of these particles reduces the

distance travelled in the axial direction of the fracture. The particles need to travel large distances in the axial direction to reach deep into the fracture and increase the oil recovery. Thus, the settling rate of the 'proppant' particles needs to be reduced to increase the effectiveness of the fracturing process. A commonly used polymeric solution to transport the particles is a borate cross-linked guar gum solution [3]. The non-Newtonian properties of these solutions play an important role in their particle-transport capabilities.

In Stokes flow of Newtonian fluids, the settling rate of a spherical particle is not affected by an imposed shear flow in the orthogonal direction to gravity, which is termed a *cross-shear flow* in the paper. But in non-Newtonian fluids, the settling rate is dependent on the shear-thinning (i.e. viscosity reduction with increase of shear rate) as well as the elastic properties of the fluid. There have been both single sphere experiments [4] as well as experiments in more concentrated suspensions [5,6] to determine the settling rate of particles sedimenting in the vorticity direction of an imposed

shear flow. The single sphere experiments [4] were performed in an aqueous mixture containing polyacrylamide which is a Boger fluid i.e. it is primarily elastic with modest shear-thinning. The concentrated suspension experiments were performed using both Boger fluids [5] as well as borate cross-linked guar gum solutions [6]. The guar gum solutions have both shear-thinning and elastic properties [6]. The settling rate of the sphere is reduced by 50% in Boger fluids due to the cross-shear flow [4]. The reduction in settling rate is more drastic for concentrated suspensions in Boger fluids [5]. But perhaps surprisingly the settling rate increases with the cross-shear flow in elastic guar gum solutions. Thus, the fluid rheology as well as particle concentration are important factors determining the settling rate of the particles under these conditions.

The problem of interest in this paper, namely sedimentation in viscoelastic fluids under imposed shear, has not been fully understood. The experiments for concentrated suspension [5,6] of spherical particles in various viscoelastic liquids have shown that the settling rate can be reduced or increased depending on the rheology of the fluid. The difference between the results of the single sphere experiments [4] and concentrated suspension experiments [5,6] indicate that the particle concentration is very important in determining the settling rates. The problem of single sphere in weakly viscoelastic fluid was investigated by Housiadas and Tanner [7] using perturbation theory which provided some insight about the role of elasticity. Padhy et al. [8] investigated this problem in elastic Boger fluids using numerical simulations. They found the decrease in settling rates observed in the experiments and proposed a mechanism for the effect of elasticity on the settling rates. We study the effect of fluid rheology on settling rate especially the increase in settling rate in elastic guar gum solutions. We also examine the effect of walls in this sedimentation problem as our previous calculations [8] suggested that wall effects played a primary role in explaining the discrepancy between the theory of Housiadas and Tanner [7] and the available experiments [4].

In this context, it is well known that the presence of walls changes the drag on a sedimenting sphere in a Newtonian fluid. The drag correction factor for Newtonian fluids at *Re* = 0 can be obtained using Faxen's law [9]. There has been significant work done to determine the wall effects in elastic fluids under simple sedimentation [10–14]. There is a well known reduction for weak elastic effects in the drag correction factor from the Newtonian value due to the fluid elasticity. But as fluid elasticity is increased, the drag correction factor reaches a plateau and begins to increase. The wall effects on a particle in a viscoelastic shear flow alone have been investigated by Avino et al. [15] using numerical simulations. They studied the dynamics of the particle under imposed confined shear flow. They found particle migration towards the closest wall due to the confinement and viscoelasticity of the fluid. They extended the analysis for time dependent shear flow and obtained many features of previous experimental results [16]. In the present study, we are concerned with the effect of confinement on a sphere sedimenting in a viscoelastic cross-shear flow.

Thus, we study via numerical simulation the problem of a sedimenting sphere with cross-flow in a viscoelastic medium but this time for a broader range of fluid rheology than was considered in our previous work [8]. The simulations are performed for elastic guar gum solutions as well as Boger fluids. The parameters for the simulations are determined by fitting the rheological data measured in experiments [4,6]. The drag coefficients computed from the simulations are directly related to the settling rate of a sphere. The simulation results, indeed, show the increase in settling rate observed in the experiments for elastic guar gum solutions. We analyze these results to determine the effect of shear-thinning and elasticity on the setting rate as discussed in Section 5.1. The effect of walls on the reduction in sedimentation speed in elastic fluids is examined in Section 5.2.

2. Problem formulation

2.1. Problem definition

One can refer to our previous paper [8] for details of the problem set up, but we will review it briefly here. The problem consists of a freely sedimenting sphere moving with constant speed U_∞ under the action of gravity in a cross-shear flow. An inertial frame of reference is attached to the sphere and simulations are performed in this frame of reference. A fluid with uniform velocity of U_i (where $U_i = -U_\infty \tilde{g}_i$, $\tilde{g}_i$ is a unit vector in the direction of gravity and from Fig. 1, $\tilde{g}_i \equiv \delta_{i1}$) is flowing past a stationary sphere. A no slip boundary condition is applied at the upper and lower plates and these are moved with a speed S in opposite directions. This enforces the cross-shear flow in the problem. The torque on the sphere is constrained to be zero. A rotational velocity, ω_i, is applied to the sphere (only ω_1 is non-zero by symmetry) so that the condition on the torque is satisfied.

2.2. Governing equations

The flow of an incompressible fluid containing polymer additives is governed by the equations of conservation of mass and momentum. The non-dimensionalized forms of these equations are given by:

$$\frac{\partial u_i}{\partial x_i} = 0 \tag{1}$$

$$\frac{\partial u_i}{\partial t} + u_j \frac{\partial u_i}{\partial x_j} = -\frac{\partial p}{\partial x_i} + \frac{\beta}{Re}\frac{\partial^2 u_i}{\partial x_j \partial x_j} + \frac{1-\beta}{Re}\frac{\alpha}{Wi}\frac{\partial \tau_{ij}^P}{\partial x_j} \tag{2}$$

where τ_{ij}^P is the stress due to the polymers. The inlet velocity magnitude (U_∞) and the sphere diameter (D) are used to make the variables non-dimensional. The polymer stress and the pressure have been made non-dimensional using μ_p/λ and ρU_∞^2 respectively where λ is the characteristic relaxation timescale of the polymer and μ_p is the polymer contribution to the viscosity. The non-dimensional parameters of interest are the shear Weissenberg number ($Wi = \lambda\dot{\gamma}$), the flow Weissenberg number ($\theta = \lambda U_\infty/D$) and the Reynolds number ($Re = \rho U_\infty D/(\mu_s + \mu_p)$) where $\dot{\gamma}$ is the characteristic shear rate applied across the cell in the $x_2 - x_3$ plane and μ_s is the solvent contribution to the viscosity. The other parameters of note are $\beta = \mu_s/(\mu_s + \mu_p)$ and $\alpha = \dot{\gamma}D/U_\infty = Wi/\theta$.

The two constitutive models used in the paper are the FENE-P model and the single mode Giesekus model [17]. The FENE-P model is used for the constitutive equations of the Boger fluids (Section 5.2). The polymer stress term in Eq. (2) using the FENE-P model is given by [18],

$$\tau_{ij}^P = \frac{c_{ij}}{1 - \frac{c_{kk}}{L^2}} - \delta_{ij} \tag{3}$$

where L is the dimensionless maximum polymer extensibility and c_{ij} is the dimensionless averaged polymer conformation tensor with both made dimensionless using the equilibrium Hookean spring length. The equilibrium Hookean spring length is $(kT/H)^{(1/2)}$ where T is the absolute temperature, k is Boltzmann's constant and H is
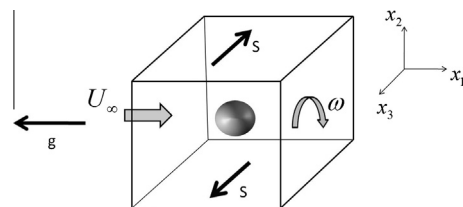

Fig. 1. Schematic of the problem used for simulation.

the Hookean spring constant for an entropic spring. The polymer conformation tensor is defined as the preaveraged diadic product of the polymer end-to-end vector. The transport equation governing the conformation tensor is given by,

$$\frac{\partial c_{ij}}{\partial t} + u_k \frac{\partial c_{ij}}{\partial x_k} - c_{ik}\frac{\partial u_j}{\partial x_k} - c_{kj}\frac{\partial u_i}{\partial x_k} = -\frac{\alpha}{Wi}\tau_{ij}^P \tag{4}$$

The single mode Giesekus model [17] is used for the constitutive equations of the guar gum solutions(Section 5.1). In this case, the polymer stress term in Eq. (2) is given by,

$$\tau_{ij}^P = c_{ij} - \delta_{ij} \tag{5}$$

The conformation tensor is governed by the transport equation given by,

$$\frac{\partial c_{ij}}{\partial t} + u_k \frac{\partial c_{ij}}{\partial x_k} - c_{ik}\frac{\partial u_j}{\partial x_k} - c_{kj}\frac{\partial u_i}{\partial x_k} = -\frac{\alpha}{Wi}\tau_{ij}^P - \frac{\alpha\zeta}{Wi}\tau_{ik}^P\tau_{kj}^P \tag{6}$$

where ζ is the dimensionless mobility parameter [17].

The velocity, pressure and polymer conformation can be calculated from the set of 10 coupled partial differential equations which are provided by Eqs. (1), (2) along with either (4) or (6) in conjunction with the expression for the polymer stress term given by Eq. (3) or (5). The numerical method we use for solving the equations is described in detail in Richter et al. [19] and in our previous work [8]. A fully three dimensional parallel code based on an unstructured finite volume formulation for incompressible Newtonian flow named CDP is used as the basic code. This Newtonian flow solver was developed at Stanford's Centre for Turbulence Research. The code for the solution of the viscoelastic flow is obtained by addition of the polymer stress term (either FENE-P or Giesekus) as a volumetric source term in the Newtonian momentum solver. The conformation evolution equations are solved as six coupled scalar transport equations. This code is capable of solving problems with a wide range of Reynolds and Weissenberg numbers [19–22].

2.3. Boundary conditions

The sphere is located at the origin of the coordinate system. The standard domain (with directions as defined in Fig. 1) has dimensions of 37.5D, 11.66D and 8.33D in the x_3, x_2 and x_1 directions, respectively. The velocities of the top and bottom plate in the x_2 direction is fixed to be $\delta_{i1} - 8.33\alpha\delta_{i3}$ and $\delta_{i1} + 8.33\alpha\delta_{i3}$ respectively with a no slip boundary condition. The velocity at the inlet boundary where fluid is entering the domain in the x_1 direction is given by $\delta_{i1} - (\alpha x_2)\delta_{i3}$. A convective outlet condition is applied where the fluid is leaving the domain in the x_1 direction. The velocity there is extrapolated from the interior cells assuming fully developed flow and maintaining the overall mass balance. A no slip boundary condition is imposed at the surface of the sphere with a fixed velocity corresponding to the solid body rotation of the sphere with rotational velocity ω_1. The value of ω_1 is found by iteration using the secant method until the magnitude of the non-dimensional torque value ($T = 2\overline{T}/(\pi(\mu_s + \mu_p)D^3\dot{\gamma})$, where $\overline{T}$ is the dimensional torque value) becomes less than 0.01. The secant method consists of updating the rotational velocity after every time interval of λ according to the Eq. (7) where k is the time step number.

$$\omega_1^{(k+1)} = \omega_1^{(k)} - \frac{\omega_1^{(k)} - \omega_1^{(k-1)}}{T^{(k)} - T^{(k-1)}}T^{(k)} \tag{7}$$

At the inlet, the analytical solution of c_{ij} for plane Couette flow of a FENE-P fluid is imposed [23] for the Boger fluid (Section 5.2). For the guar gum solutions (Section 5.1), an equilibrium distribution for c_{ij}, i.e. $c_{ij} = \delta_{ij}$, is imposed at the inlet and it is allowed to develop with the flow. In the x_3 direction a periodic boundary condition is applied both for velocity and c_{ij}. All the simulations

were carried out at $Re = 0.01$. The time step size Δt was chosen to be $4.261 \times 10^{-5}\lambda$ for the Boger fluid (Section 5.2) and $1.602 \times 10^{-3}\lambda$ for the guar gum solutions (Section 5.1) for obtaining stable simulation results. We discuss the steady state results for the problem in this paper. The steady state condition was determined to be reached when the drag value on the sphere as well as the L_∞ norms of τ_{11}, τ_{11}^P, τ_{12}^P and τ_{13}^P in the domain changed by less than 1% in a time interval of λ. Here $\tau_{1k} = \frac{\partial u_1}{\partial x_k} + \frac{\partial u_k}{\partial x_1}$ is the non-dimensional viscous stress on the sphere.

2.4. Mesh

The simulations are performed in a domain with dimensions of 37.5D, 11.66D and 8.33D in the x_3, x_2 and x_1 directions, respectively on a unstructured grid containing 8.725 million tetrahedral elements. The mesh is comprised of smaller elements near the sphere to resolve the polymer stress gradients and larger elements farther from the sphere. The tetrahedral mesh has a smallest element size of 0.01D. The mesh used for investigating the effect of walls (Section 5.2) has the same mesh resolution with dimensions of 37.5D, 5D and 8.33D in the x_3, x_2 and x_1 directions, respectively. This mesh contains 6.259 million tetrahedral elements. The dimensions and the mesh resolution of the mesh were changed to check for grid convergence and the effect of domain size. The domain used for these simulations has dimensions of 37.5D, 12.5D and 8.33D in the x_3, x_2 and x_1 directions, respectively and contains 6.08 million tetrahedral elements. The smallest element has a size of 0.015D. The results from the simulations carried out in both the meshes are in good agreement (Section 5.1).

3. Code verification

The viscoelastic code for Giesekus model is verified by running the simulation for steady, fully-developed Poiseuille flow through a parallel plate channel. An analytical solution for this flow has been previously derived by Schleiniger & Weinacht [24]. Our simulations is carried out in a mesh with quadrilateral elements of size 0.02h where 2h is the separation between the two infinite parallel plates. The parameters for the Giesekus model are chosen to be $\zeta = 0.1$ and $\beta = 0.9$ as a test case.

The variables are made non-dimensional using the scaling given by Schleiniger & Weinacht [24] for the analytical solutions. The velocity and length scale used are $\sqrt{hG/\rho}$ and channel half-height (h) respectively where G is the applied pressure gradient. Thus, in this case the flow Weissenberg number is given by $\theta = \lambda\sqrt{G/(h\rho)}$. The Reynolds number is given by $Re = h\sqrt{\rho Gh}/\mu_p$ following the definition in Schleiniger & Weinacht [24]. The parameters used in the simulations are $\theta = 1.414$ and $Re = 17.67$. The comparison between the computed and analytical results for the non-dimensional velocity and polymer stress tensor components is shown in Fig. 2(a)–(c). The match between the computed results and the analytical profiles is excellent. The code for the Giesekus model is further verified by comparison to the results by Snijkers et al. [25] for rotation rate of a freely rotating sphere in viscoelastic shear flow, which is presented in our previous work [8]. The verification studies for the FENE-P model code has been performed earlier and are described in Richter et al. [19] and Padhy et al. [8].

4. Fitting model parameters to experimental data

4.1. Guar gum solution

The single mode Giesekus model [17] is used to model the constitution of the guar gum solution. The parameters for the model are obtained by fitting the experimental rheological properties of
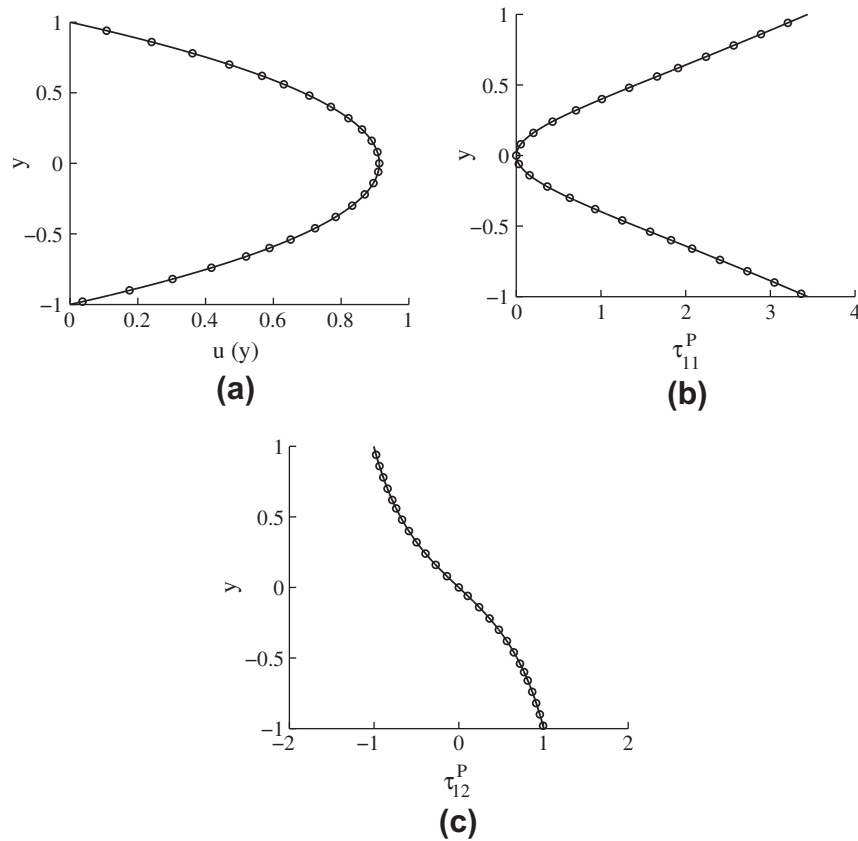
Fig. 2. Comparisons of analytic (—) and simulated (○): (a) streamwise velocity u and polymer stress tensor components, (b) τ_{11}^P and (c) τ_{12}^P for $Re = 17.67$, $\theta = 1.414$, $\beta = 0.9$ and $\zeta = 0.1$. (Note that the simulated result for only 1 in every 4 mesh elements is plotted for clarity in the plot.)
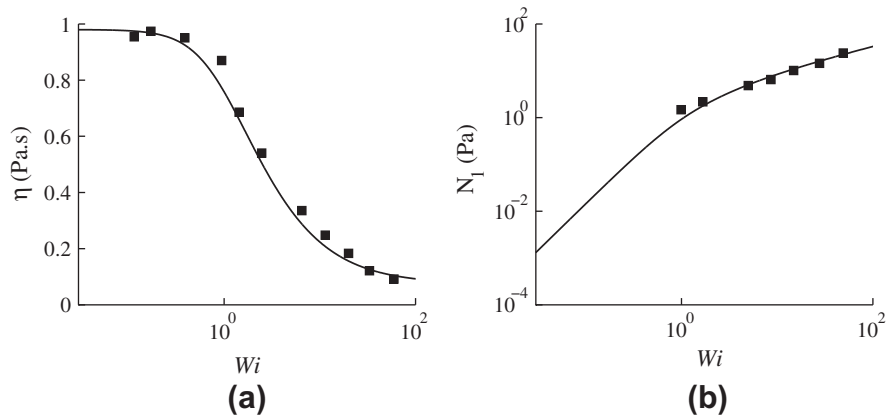
Fig. 3. Fits to experimental data of 31 ppm Borate cross-linked guar gum solution: (a) steady shear data for viscosity and (b) steady shear data for first normal stress difference. Solid line, Single Mode Giesekus model; ■, experimental data of Tonmukayakul et al. [6].

31 ppm Borate cross-linked guar gum solution measured by Tonmukayakul et al. [6]. The parameters so obtained after the fitting procedure were $\eta = 0.98$ Pa s, $\lambda = 1.2487$ s, $\alpha = 0.1769$ and $\beta = 0.076$. The comparison of the fit and experimental data is shown in Fig. 3. The guar gum solutions shear thin appreciably over the range of shear rates examined.

4.2. Boger fluid

The FENE-P model is used to represent the constitutive equations for the Boger fluid. The parameters for this model are obtained by fitting the experimental rheological properties of 1% PAA solution (in a mixture of water and corn syrup) measured by

Tonmukayakul et al. [5]. The relaxation time is obtained by fitting the experimental data for first normal stress difference obtained by the stress relaxation test. The parameters so obtained after the fitting procedure were $\eta = \mu_p + \mu_s = 1.249$ Pa s, $\lambda = 0.469$ s, $L = 31.6$ and $\beta = 0.785$. The comparison of the fit and experimental data is shown in Fig. 4. Note that the results correspond to modest shear thinning of η over the experimental range of shear rate.

5. Results and discussion

5.1. Guar gum solutions

We discuss the drag coefficient, C_d, defined by,
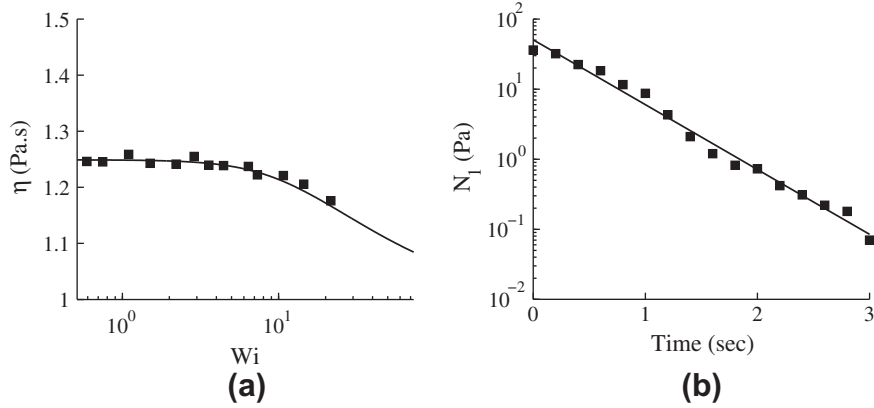
Fig. 4. Fits to experimental data of 1% PAA solution: (a) steady state viscosity and (b) transient first normal stress difference. Solid line, FENE-P model; ■, experimental data of Tonmukayakul et al. [5].
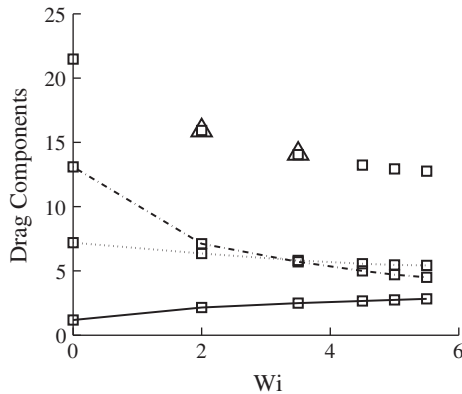
$$C_d = \frac{2F_1}{(\mu_p + \mu_s)U_\infty D} \tag{8}$$

where F_1 is the force experienced by the sphere in the x_1 direction. As in our previous paper [8], the drag coefficient is further broken down into the individual components associated with the different type of stresses on the sphere. The total drag coefficient is thus given by:

$$C_d = \underbrace{-2Re \iint_S p n_1 dS}_{\text{form drag}} + \underbrace{4\beta \iint_S \left(\frac{\partial u_1}{\partial x_k} + \frac{\partial u_k}{\partial x_1}\right) n_k dS}_{\text{viscous drag}} + \underbrace{2\frac{1-\beta}{Wi}\alpha \iint_S \tau_{1k}^P n_k dS}_{\text{polymer drag}}$$

$$\tag{9}$$

where n_j is the unit outward normal vector on the surface of the sphere, p is made dimensionless with ρU_∞^2 and dS is the non-dimensional differential area element (non-dimensionalized by D^2). The simulations were carried out on two different unstructured meshes to check grid convergence. The drag coefficients at different cross-shear Weissenberg numbers are shown in Fig. 5 for these two meshes. There is little difference between the results for both the meshes and the finer mesh is used for all further calculations we discuss.

The drag coefficients decrease with an increase in Wi, which is qualitatively in agreement with the experiments. The components of the drag coefficients are also presented in Fig. 5. A key finding is that the drag contribution due to the polymer stresses is the dominant contribution. The contributions due to the polymer stresses decrease with increase in Wi. There is also an increase in the con-

tributions due to the viscous stresses but this is not enough to offset the decrease due to the polymer stresses. Thus, the total drag coefficients decrease with an increase in Wi.

The mechanism for the decrease in the drag coefficients is further investigated by analyzing the components of viscous and polymer stresses. The components of these stresses are transformed into a spherical coordinate system which is shown in Fig. 6. A spherical coordinate system helps to analyze the stresses as at each point since the shear and normal stresses are aligned with the unit normals for the spherical coordinate system. The unit normals in r, ψ and ϕ directions are represented by $\hat{e}_r, \hat{e}_\psi$ and $\hat{e}_\phi$ respectively. The contribution to the drag coefficient due to the polymer stresses is broken into the individual contributions due to each of the stress components $\left(\tau_{rr}^P, \ \tau_{r\psi}^P, \ \tau_{r\phi}^P, \ \tau_{\psi\psi}^P, \ \tau_{\phi\phi}^P \ \text{and} \ \tau_{\psi\phi}^P\right)$. The drag contribution due to the polymer stresses is given by:

$$\underbrace{C_{d,poly}}_{\text{polymer drag}} = \underbrace{2\frac{1-\beta}{Wi}\alpha \iint_S \tau_{rr}^P \hat{e}_r \sin\psi \cos\phi dS}_{\text{drag due to } \tau_{rr}}$$

$$+ \underbrace{2\frac{1-\beta}{Wi}\alpha \iint_S \tau_{r\phi}^P (\hat{e}_\phi \sin\psi \cos\phi - \hat{e}_r \sin\phi)dS}_{\text{drag due to } \tau_{r\phi}^P}$$

$$+ \underbrace{2\frac{1-\beta}{Wi}\alpha \iint_S \tau_{r\psi}^P (\hat{e}_\psi \sin\psi \cos\phi + \hat{e}_r \cos\psi \cos\phi)dS}_{\text{drag due to } \tau_{r\psi}^P}$$

$$+ \underbrace{2\frac{1-\beta}{Wi}\alpha \iint_S \tau_{\psi\psi}^P \hat{e}_\psi \cos\psi \cos\phi dS}_{\text{drag due to } \tau_{\psi\psi}^P}$$

$$- \underbrace{2\frac{1-\beta}{Wi}\alpha \iint_S \tau_{\phi\phi}^P \hat{e}_\phi \sin\phi dS}_{\text{drag due to } \tau_{\phi\phi}^P}$$

$$+ \underbrace{2\frac{1-\beta}{Wi}\alpha \iint_S \tau_{\psi\phi}^P (\hat{e}_\phi \cos\psi \cos\phi - \hat{e}_\psi \sin\phi)dS}_{\text{drag due to } \tau_{\psi\phi}^P} \tag{10}$$

A similar approach is used to break down the drag contribution due to the viscous stresses. The viscous stress components in the spherical coordinate system are represented by $\tau_{rr}, \tau_{r\psi}, \tau_{r\phi}, \tau_{\psi\psi}, \tau_{\phi\phi}$ and $\tau_{\psi\phi}$. The three largest drag contribution by the stress components are shown in Fig. 7. The dominant contribution for $Wi > 2$ comes from the $\tau_{r\phi}^P$ component of the polymer stress and the $\tau_{r\phi}$ component of the viscous stress. These components are further investigated by analyzing the stress distributions on the surface of the sphere.
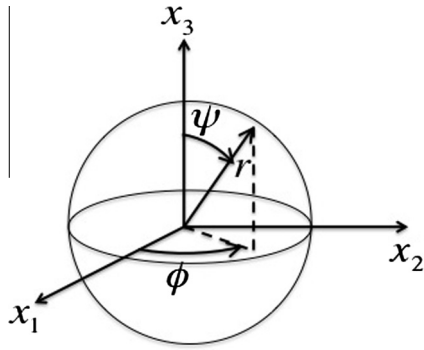

Fig. 5. Drag coefficients and components ($\theta = 0.15$). □, total drag (finer mesh); △, total drag (coarser mesh); –·...□...·–, polymer drag; ·····□·····, form drag; –□–, viscous drag.

Fig. 6. Spherical coordinate system to represent components of viscous and polymer stresses.
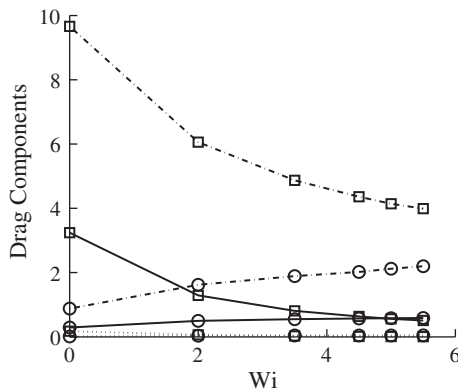
Fig. 7. Components of viscous and polymer drag ($\theta = 0.15$). $-\cdot\cdot\cdot\boxdot\cdot\cdot\cdot-$, drag due to $\tau_{r\phi}^P$; $\cdot\cdot\cdot\cdot\cdot\boxdot\cdot\cdot\cdot\cdot\cdot$, drag due to τ_{rr}^P; $-\boxminus-$, drag due to $\tau_{r\psi}^P$; $-\odot-$, drag due to $\tau_{r\phi}$; $\cdot\cdot\cdot\odot\cdot\cdot\cdot$, drag due to τ_{rr}; $-\ominus-$, drag due to $\tau_{r\psi}$.

The plot of the drag contribution by $\tau_{r\phi}^P$ component of the polymer stress $\left(\tau_{r\phi}^P(\hat{e}_\phi \sin\psi \cos\phi - \hat{e}_r \sin\phi)\right)$ on the surface of the sphere is shown in Fig. 8. We present the distributions on the "right side" of the sphere which is the part of the sphere in the positive half-space in the x_3 direction. Distributions for two different cases at $Wi = 3.5$ are shown i.e. the case with only uniform flow (Fig. 8(a)) and the case with both uniform flow and orthogonal shear flow (Fig. 8(b)). The distribution is not symmetric for the case with both uniform flow and cross-shear flow. This leads to a net drag in the x_1 direction. This effect is similar to the effect for viscous stresses, which was reported in Padhy et al. [8] for Boger fluids. The distribution for the case with only uniform flow has positive contributions only. The total drag is obtained by integrating the profiles shown in Fig. 8. The integral of the profile for the case with only uniform flow gives a larger value than the integral of the profile for the case with both uniform flow and shear flow because there are no negative contributions for the case with only uniform flow. This has been shown earlier in Fig. 5 where the polymer drag component decreased as Wi is increased from 0 to 3.5. Thus, the shear flow reduces the drag created by the polymers. Since the polymer is shear-thinning, the cross-shear flow reduces the solution viscosity that ultimately leads to the decrease in the polymer drag component. We now discuss the effect of the shear-thinning characteristics of the guar gum solutions on the drag contribution due to the polymer stresses.

Simulations are performed for three different values of β ($\beta = 0.076$, 0.5, 0.8) with all other parameters for the Giesekus model being kept constant. Note here that the only fluid that exists in reality is $\beta = 0.076$. The rest is a parameter study. The plot for the steady viscosity is shown in 9(a). It is important to note that the polymer contribution to total viscosity, $\mu_p = nkT\lambda = (1 - \beta)\mu_{total}$, is related to the parameter β. Thus, the concentration of polymer in the solution is determined by β. As the amount of polymer present in the solution increases (β decreases) the solution shear-thins increasingly because the polymer contribution is shear-thinning. The results for the drag coefficients for different values of β are shown in Fig. 9(b). The drag coefficients decrease with an increase in Wi for all the cases. But the decrease in the drag coefficients is less significant for the case with a higher value of β. Thus, as the solutions increasingly shear-thin the decrease in the drag coefficients is also increased.

The drag coefficient contributions due to the polymer stresses, viscous stresses and the pressure are calculated using Eq. (9) and presented in Fig. 9(c). The individual contributions to the drag are shown in Fig. 9(c) for $\beta = 0.076$ and $\beta = 0.8$. The drag contribution due to the polymer stresses decreases and the drag contribution due to the viscous stresses increases for both values of β as Wi is increased. The polymer drag component dominates for $\beta = 0.076$. Thus, the decrease in the polymer drag component more than offsets the increase in the viscous drag component and the total drag coefficient decreases. But for $\beta = 0.8$, the viscous drag component dominates. Thus, the increase in the viscous drag component almost cancels the decrease in the polymer drag component and there is a small decrease in the total drag coefficient.

Padhy et al. [8] have shown that the polymers in the solution indirectly increase the viscous drag component. This phenomenon is also present in guar gum solutions for all values of β, i.e. there is an increase in the viscous component of the drag. But this increase in the viscous drag component is overcome by the decrease in polymer drag component in the elastic guar gum solutions, which are investigated in this paper. Due to the shear thinning characteristics of the guar gum solutions the polymer drag component decreases. This effect was not present in the Boger fluids as Boger fluids are primarily elastic and shear thin very little. Thus, in Boger fluids, the indirect increase in the viscous drag component leads to an increase in the total drag coefficient.

Thus, the competing effects are the decrease in the polymer drag component due to shear-thinning and the indirect increase in the viscous drag component due to the polymers. If the amount of polymers present is large (β small), the decrease in the polymer drag component dominates and we get an overall decrease in the drag coefficient. This is true for the elastic guar gum solutions which are investigated in this paper as the value of β is 0.076 for these solutions. On the other hand, if the amount of polymers present is too small ($\beta \sim 1$), there is not an indirect increase in the viscous drag component as the solution is essentially a Newtonian fluid. It follows, that there is an optimum value for the amount of polymer in the guar gum solutions to create an increase in drag coefficients. At the optimum value of β, the increase in the viscous drag component overwhelms the decrease in the polymer drag component. In Boger fluids, the competing effect of decrease in polymer drag component is nearly absent as Boger fluids do not shear-thin appreciably and thus there is nearly always an increase in the drag coefficients for these fluids.

The shear-thinning effect in the guar gum solutions is further verified by rescaling the forces on the sphere. We scale the force on the sphere due to the viscous stresses by the Newtonian component of the viscosity (μ_s) and the force on the sphere due to the polymer stresses by the polymer viscosity (μ_p). Thus, the viscous and polymer drag components are now given by:

$$C_d^N = \frac{2F_1^N}{\mu_s U_\infty D} \tag{11}$$

$$C_d^P = \frac{2F_1^P}{\mu_p U_\infty D} \tag{12}$$
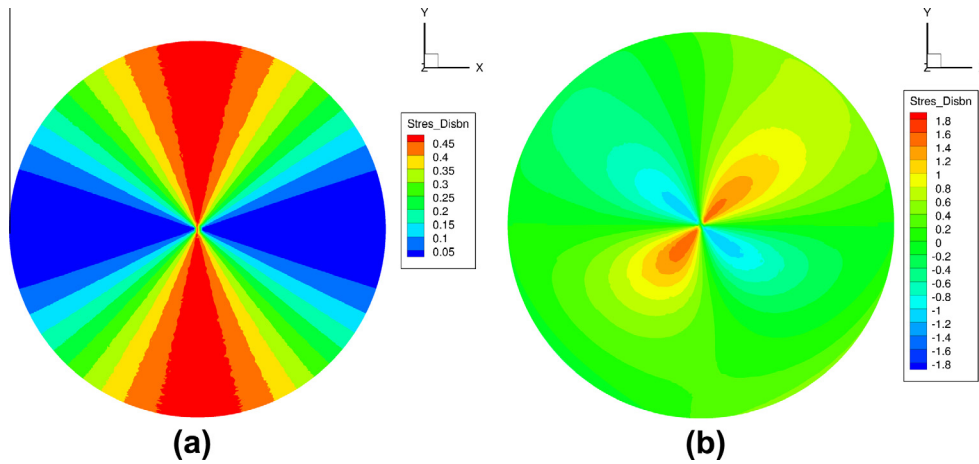
Fig. 8. Contour plots of drag contribution by $\tau_{r\phi}^{P}$ on right side of the sphere: (a) only uniform flow at Wi = 3.5 and (b) both uniform flow and shear flow at Wi = 3.5.
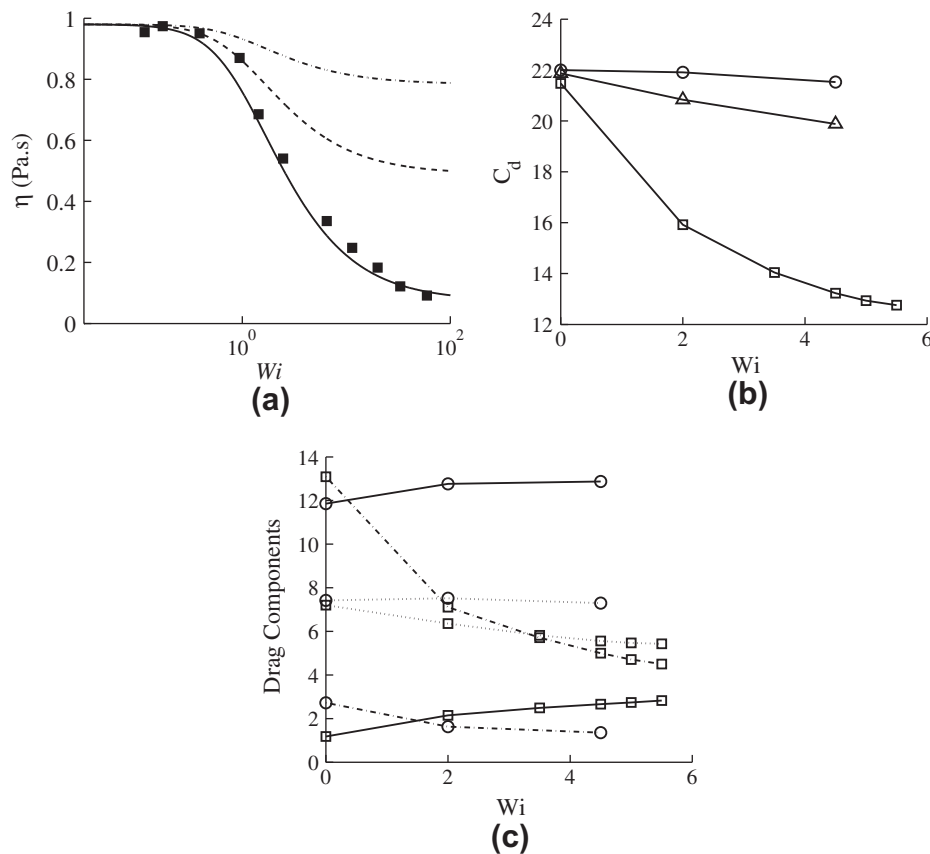
Fig. 9. (a) Steady shear viscosity for different β. ■, experimental data of Tonmukayakul et al. [6]; ——, β = 0.076; - - - -, β = 0.5; -·--·-, β = 0.8. (b) Drag coefficients for different β. □, β = 0.076; △, β = 0.5; ○, β = 0.8. (c) Drag components for β = 0.076 & β = 0.8. -·- · · □ · · -·-, polymer drag (β = 0.076); · · · · · □ · · · ·, form drag (β = 0.076); –⊟–, viscous drag (β=0.076); ·-⊙-·, polymer drag (β = 0.8); · · ·⊙· · ·, form drag (β = 0.8); –⊖–, viscous drag (β = 0.8).

where F_1^N and F_1^P are the forces experienced by the sphere in the x_1 direction due to the viscous stresses and polymer stresses respectively. The rescaled polymer and viscous drag components for β = 0.076 and β = 0.8 are shown in Fig. 10(a). At Wi = 0, the rescaled polymer and viscous components are almost equal for both values of β. This is due to the fact that the effect of polymers is minimal at Wi = 0 and the solution behaves as a Newtonian fluid. As Wi is increased, the polymers in the solution start to shear thin and the

polymer drag component decreases. The decrease in the rescaled polymer drag component is similar for both values of β. This is due to the fact that only the amount of polymers changes for different β but the shear-thinning characteristics of the polymers remain the same. Thus, the polymer forces on the sphere scaled by the respective polymer viscosities for different values of β follow the same behavior. It is also interesting to note that the increase in the rescaled viscous drag component is larger for β = 0.076. The
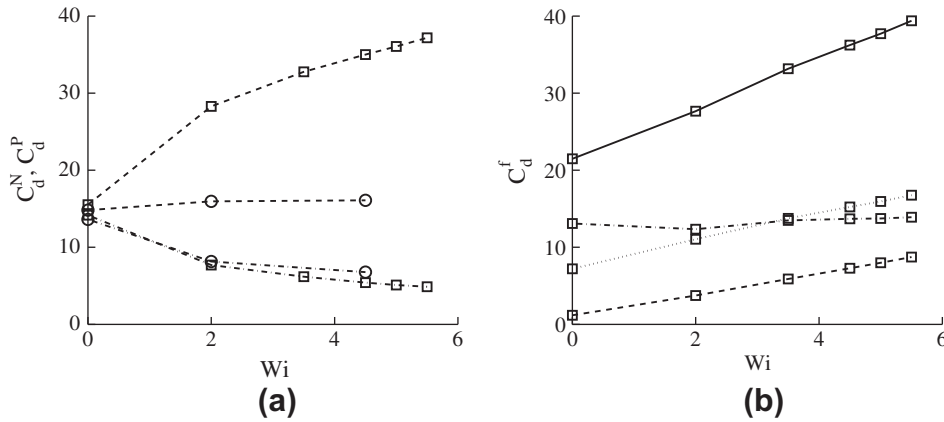
Fig. 10. (a) Rescaled viscous and polymer drag components (Eq. (12)). --···□···--, polymer drag ($\beta = 0.076$); - - ⊟ - -, viscous drag ($\beta = 0.076$); --⊙--, polymer drag ($\beta = 0.8$); --⊖- -, viscous drag ($\beta = 0.8$). (b) Rescaled drag coefficient (Eq. (13)) ($\beta = 0.076$). –⊟–, total drag; --···□···--, polymer drag; ·····□·····, form drag; - - ⊟ - -, viscous drag.

amount of polymer present in the solutions is increased for $\beta = 0.076$ and this leads to a larger increase in the viscous drag component, i.e. a larger "indirect" effect.

The total viscosity of the solution decreases appreciably with Wi for the guar gum solutions. The drag forces are rescaled by using the viscosity of the solution at the particular Wi for which the drag coefficient is being calculated. This eliminates the effect of the decrease of the polymer contribution to total viscosity with Wi, on the drag coefficients.The drag coefficient is now defined by:

$$C_d^f = \frac{2F_1}{\mu_f U_\infty D} \tag{13}$$

where F_1 is the force experienced by the sphere in the x_1 direction and μ_f is the solution viscosity at a particular Wi. The solution viscosity at each Wi is obtained from the rheological fit and it is used for scaling the drag forces at that Wi. The rescaled total drag coefficients as well as the drag components are shown in Fig. 10(b) for $\beta = 0.076$. The rescaled total drag coefficients increase with an increase in Wi. The polymer drag component is almost constant and the viscous drag component increases with an increase in Wi. This behavior is similar to the behavior of the Boger fluids. The shear-thinning effect of the guar gum solutions is eliminated with this rescaling. Thus, the guar gum solutions show the same behavior as that of the Boger fluids in which shear-thinning is absent. This is also verified from the fact that the rescaled polymer drag component does not decrease as shear-thinning is eliminated by rescaling.

5.2. Effect of walls on drag coefficients in Boger fluids

Housiadas and Tanner [7] proposed a theoretical model to predict the drag coefficient for $\theta \ll 1$ using perturbation theory. One of the reasons for the mismatch between their results and the experimental results by van den Brule and Gheissary [4] was suggested [8] to be due to the effect of the walls in the shear gradient (x_2) direction but a quantitative explanation has not been provided. We investigate the effect of walls on drag coefficients, as the walls in the shear gradient (x_2) direction are placed closer to the sphere.

Simulations are performed for different values for D/W where D is the diameter of the sphere and W is the separation between the walls in the x_2 direction (Fig. 1). We use the FENE-P model with the parameters obtained in Section 4.2 to represent the Boger fluid. In Fig. 11(a), the ratio of drag coefficient, C_d/C_0, is plotted as a function of Weissenberg number for $\theta = 0.1$ for three different values of D/W. The drag coefficients are larger for larger values of D/W. In other

words, the increase in the drag coefficients (decrease in the settling rate) is larger, as the walls are placed closer to the sphere.

The individual components associated with the different type of stresses on the sphere is calculated using Eq. (9) presented earlier. In Fig. 11(b), the drag contributions due to the polymer stresses, viscous stresses and the pressure are shown for different values of D/W. The individual contributions to the drag with respect to the contributions at $Wi = 0$ are presented. The polymer drag component is almost constant and the viscous drag component increases with Wi at both values of D/W. But the increase in the viscous drag component is larger for $D/W = 0.2$. Thus, there is a larger increase in the drag coefficients as walls are placed closer to the sphere primarily because there is a larger increase in the viscous drag component, which is the dominant contributor to drag.

The drag contributions from the dominant polymer and viscous stress components for different values of D/W are shown in Fig. 11(c). The dominant contribution comes from the $\tau_{r\phi}$ component of the viscous stress for high Wi. The contribution from the viscous shear stress is larger for $D/W = 0.2$. Thus, as the walls are placed closer to the sphere the mechanism of the increase in the drag remains the same but the effect is accentuated due to the interaction between the sphere and the wall.

We examine the change in the distributions of viscous shear stress ($\tau_{r\phi}$) around the sphere by the walls. The distribution of $\tau_{r\phi}$ component of the viscous stress in the $x_1 - x_2$ plane is shown in Fig. 12. The stress distributions for two different values of D/W are shown. A few streamlines are also plotted. The viscous shear stress ($\tau_{r\phi}$) is enhanced downstream of the sphere for both values of D/W. But for the higher value of D/W, the magnitude of the increase in the viscous shear stress is much larger and extends over more of the sphere. The streamlines are visibly more closely packed when the walls are closer to the sphere. The presence of walls leads to a much larger change in the direction of the streamlines upstream and downstream of the sphere. Thus, the viscous shear stresses are present in both these locations. Note that these upstream stresses do not cancel the drag increase due to the viscous shear stresses downstream because the viscous shear stresses upstream of the sphere are not on the sphere surface.

As the walls are brought closer to the sphere, the change in the direction of the streamlines just downstream is much larger. This leads to an increase in the magnitude of viscous shear stresses. The asymmetric distribution on the sphere, which has been presented in Padhy et al. [8] now leads to more drag as the magnitude of the stresses is larger. Thus, the drag on the sphere increases as the walls are placed closer to the sphere due to the increase in viscous shear stresses downstream of the sphere.
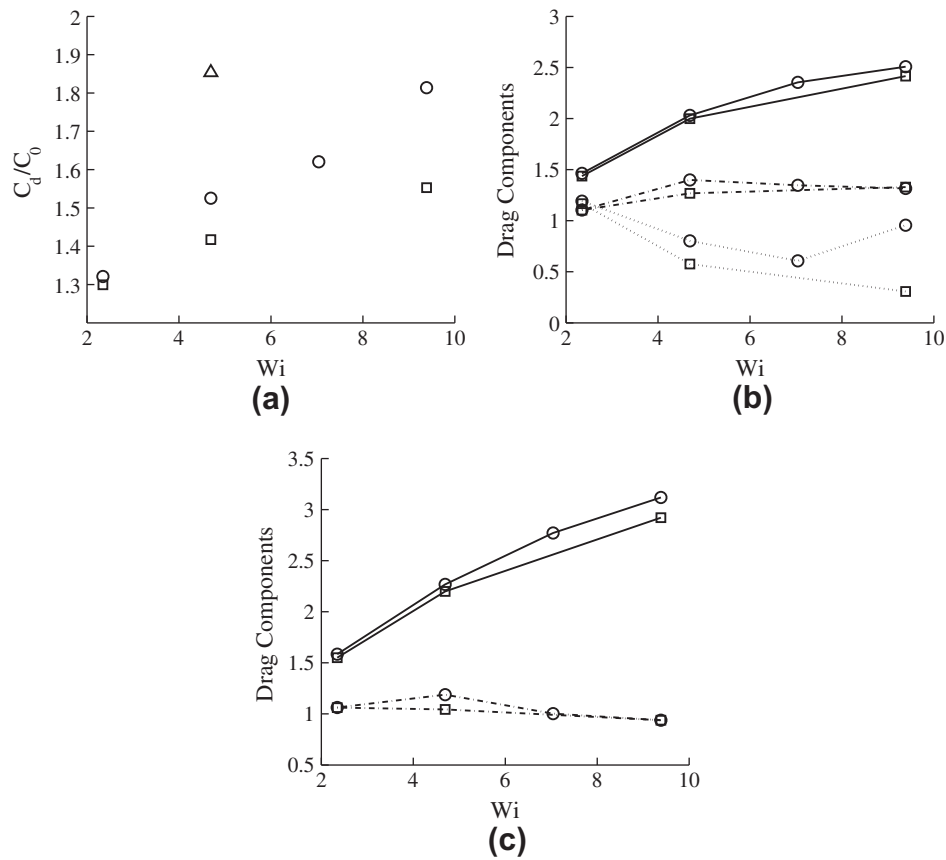
Fig. 11. (a) Effect of walls on drag coefficients($\theta = 0.1$). $\square$, $D/W = 0.08$; $\bigcirc$, $D/W = 0.2$; $\triangle$, $D/W = 0.5$. (b) Components of drag ($\square$, $D/W = 0.08$; $\bigcirc$, $D/W = 0.2$). $-\cdot-\cdot$, polymer drag; $\cdots\cdots$, form drag; $--$, viscous drag. (c) Components of viscous and polymer drag. $-\cdot-\cdot$, drag due to $\tau_{r\phi}^P$; $--$, drag due to $\tau_{r\phi}$.
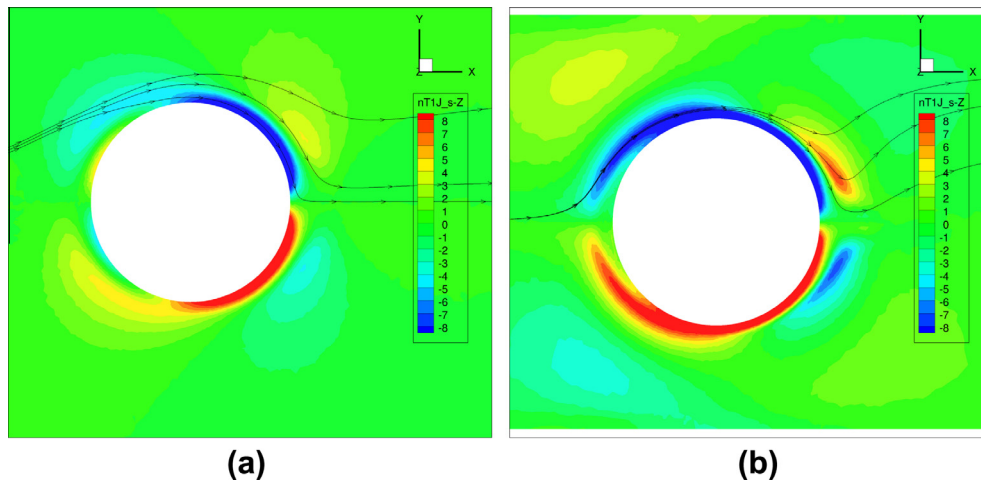
Fig. 12. Contour plot of $\tau_{r\phi}$ at $Wi = 4.69$ for different D/W: (a) $D/W = 0.08$ and (b) $D/W = 0.5$.

We found a decrease in the drag coefficients (increase in settling rate) for a sphere in elastic guar gum solutions which matches qualitatively with the experiments [6]. The decrease in the drag is larger than that observed in the experiments. A quantitative match between the experiments and the simulations is not expected because the experiments were carried out in a concentrated suspension with volume fraction of 0.2 and the simulations are performed for a single sphere. We investigated the effect of particle concentration in Boger fluids and found that as the walls are brought closer to the sphere the increase in the drag coefficients is exacerbated i.e. the effect of the elasticity in the polymers is accentuated. Thus, in a concentrated suspension, the elasticity in the polymers along with the wall effects due to the particle interactions is likely to increase the drag coefficients from the single sphere value. This may indeed explain the difference in the experimental and simulation results for the guar gum solutions, but further results including simulations at non-zero concentrations are important to verify this speculation.

6. Conclusions

We performed simulations for a sphere sedimenting in an elastic guar gum solution with a cross-shear flow. A decrease in drag with an increase in shear Weissenberg number is found which is in qualitative agreement with the experiments. The decrease in the drag (or increase in settling velocity) is due to the polymer shear stresses. The shear-thinning characteristics of the guar gum solutions lead to the decrease in the polymer drag component. The shear-thinning of the polymers tends to decrease the drag coefficients and the elasticity of the polymers tends to increase the drag coefficients. The elasticity of the polymers increases the drag coefficients indirectly through the viscous stresses. Thus, we find there is an optimum value for the amount of polymers in the solution to obtain a maximum drag coefficient (minimum sedimentation velocity). At this value the elastic "indirect" effect of the polymers overcomes the effect due to the shear-thinning of the polymers. As the walls in the shear gradient direction are placed closer to the sphere in a Boger fluid, the drag on the sphere increases. We find, that the increase in the drag is primarily due to the increase in magnitude of the viscous shear stresses ($\tau_{r\phi}$) downstream of the sphere.

Acknowledgements

References

[1] H.A. Barnes, A review of the rheology of filled viscoelastic systems, Rheol. Rev. 1 (2003) 1–36.
[2] M.J. Economides, K.G. Nolte, Reservoir Stimulation, Prentice Hall, 1989.
[3] J. Chatterji, J. Borchardt, Applications of water-soluble polymers in the oil field, J. Petro. Tech. 33 (1981).
[4] B.H.A.A. van den Brule, G. Gheissary, Effects of fluid elasticity on the static and dynamic settling of a spherical particle, J. Non-Newton. Fluid Mech. 49 (1993) 123–132.
[5] N. Tonmukayakul, J.F. Morris, R. Prud'homme, Method for estimating proppant transport and suspend ability of viscoelastic liquids, US Patent Application Publication Number US20110219856 (A1), 2011.
[6] N. Tonmukayakul, J.F. Morris, J. Bryant, M. Talbot, R. Schultz, R. Pipkin, Flow-through apparatus for testing particle laden fluids and methods of making and using same, US Patent Number US8,024,962 (B2), 2010.
[7] K.D. Housiadas, R.I. Tanner, The drag of a freely sendimentating sphere in a sheared weakly viscoelastic fluid, J. Non-Newton. Fluid Mech. 183-184 (2012) 52–56.
[8] S. Padhy, E.S.G. Shaqfeh, G. Iaccarino, J.F. Morris, N. Tonmukayakul, Simulations of a sphere sedimenting in a viscoelastic fluid with cross-shear flow, J. Non-Newton. Fluid Mech. 197 (2013) 48–60.
[9] J. Happel, H. Brenner, Low Reynolds Number Hydrodynamics: Mechanics of Fluids and Transport Processes, Martinus Nijhoff, 1973.
[10] M.T. Arigo, D.R. Rajagopalan, N.T. Shapely, G.H. McKinley, The sedimentation of a sphere through an elastic fluid. Part 1. Steady motion, J. Non-Newton. Fluid Mech. 60 (1995) 225–257.
[11] B. Yang, B. Khomami, Simulations of sedimentation of a sphere in a viscoelastic fluid using molecular based constitutive models, J. Non-Newton. Fluid Mech. 82 (1999) 429–452.
[12] W.J. Lunsmann, L. Genieser, R.A. Brown, R.C. Armstrong, Finite element analysis of steady viscoelastic flow around a sphere: calculations with constant viscosity models, J. Non-Newton. Fluid Mech. 48 (1993) 63–99.
[13] J.V. Satrape, M.J. Crochet, Numerical simulation of the motion of a sphere in a boger fluid, J. Non-Newton. Fluid Mech. 55 (1994) 91–111.
[14] H.K. Rasmussen, O. Hassager, On the sedimentation velocity of spheres in a polymeric liquid, Chem. Eng. Sci 51 (1996) 1431–1440.
[15] G.D. Avino, P.L. Maffetttone, F. Greco, M.A. Hulsen, Viscoelasticity-induced migration of a rigid sphere in confined shear flow, J. Non-Newton. Fluid Mech. 165 (2010) 466–474.
[16] B.M. Lormand, R.J. Phillips, Sphere migration in oscillatory couette flow of a viscoelastic fluid, J. Rheol. 48 (2004) 551–571.
[17] H. Giesekus, A simple constitutive equation for polymer fluids based on the concept of deformation-dependent tensorial mobility, J. Non-Newton. Fluid Mech. 11 (1982) 69–109.
[18] R.B. Bird, R.C. Armstrong, O. Hassager, Dynamics of Polymeric Liquids, second ed., Wiley, 1987.
[19] D. Richter, G. Iaccarino, E.S.G. Shaqfeh, Simulations of three-dimensional viscoelastic flows past a circular cylinder at moderate reynolds numbers, J. Fluid Mech. 651 (2010) 415–442.
[20] D. Richter, E.S.G. Shaqfeh, G. Iaccarino, Floquet stability analysis of viscoelastic flow over a cylinder, J. Non-Newton. Fluid Mech. 166 (2011) 554–565.
[21] S. Kang, G. Iaccarino, F. Ham, Dns of buoyancy-dominated turbulent flows on a bluff bodyusing the immersedboundary method, J. Comput. Phys. 228 (2009) 3189–3208.
[22] K. Mahesh, G. Constantinescu, S. Apte, G. Iaccarino, F. Ham, P. Moin, Large-eddy simulation of reactingturbulent flows in complex geometries, J. Appl. Mech. 73 (2006) 374–381.
[23] H. Yatou, Flow pattern transition accompanied with sudden growth of flow resistance in two-dimensional curvilinear viscoelastic flows, Phys. Rev. E 82 (2010) 036310. 13.
[24] G. Schleiniger, R.J. Weinacht, Steady poiseuille flows for a giesekus fluid, J. Non-Newton. Fluid Mech. 40 (1991) 79–102.
[25] F. Snijkers, G.D. Avino, P.L. Maffetttone, F. Greco, M.A. Hulsen, J. Vermant, Effect of viscoelasticity on the rotation of a sphere in shear flow, J. Non-Newton. Fluid Mech. 166 (2011) 363–372.